Electronic Supplementary Material (ESI) for ChemComm.

Supporting Information for

Bioinspired scaffolds that sequester lead ions in physically damaged high efficiency perovskite solar cells

Muhamad Z. Mokhtar[a,]*, Jiangyu He[a] , Menghan Li[a], Qian Chen[a], Jack Chun Ren Ke[a],

David J. Lewis[a], Andrew G. Thomas[a, b], Ben F. Spencer[a, b], Saif A. Haque[c] and Brian R. Saunders[a,]*

[a] *Department of Materials, University of Manchester, Manchester, M13 9PL, U.K.*

[b] *Photon Science Institute and The Henry Royce Institute, University of Manchester, Manchester, M13 9PL, UK.*

[c] *Department of Chemistry, Imperial College London, Molecular Sciences Research Hub, Wood Lane, W12 0BZ, UK.*

Corresponding authors:

Muhamad Z. Mokhtar: muhamadzulhasif.mokhtar@manchester.ac.uk

Brian R. Saunders: brian.saunders@manchester.ac.uk

EXPERIMENTAL DETAILS

Materials

$Ca(NO_3)_2{\cdot}4H_2O$ (99%), $(NH_4)H_2PO_4$ (98%), $Pb(NO_3)_2$ (99%), methyl ammonium chloride (MACl, 99.5%), isopropanol (IPA, anhydrous, 99.5%), dimethylsulfoxide (DMSO, anhydrous, 99.9%), *N*,*N*-dimethylformamide (DMF, anhydrous, 99.8%), chlorobenzene (CBZ, anhydrous, 99.5%), 2-methoxy ethanol (anhydrous, 99.5%), ethanolamine (anhydrous, 99.5%), 4-*tert*-butylpyridine (96%), lithium bistrifluoromethanesulfonimidate (LiTFSI, 99.95%), titanium isopropoxide (TIP, 99.9%), poly(methyl methacrylate) (PMMA, molecular weight 15,000 g/mol), Terpineol (99.9%) and ethylcellulose (10 cP) were all purchased from Aldrich and used as received. PbI_2 (Tokyo Chemical Industry, 99.9%), TiO_2 nanoparticles (NPs) (Dyesol 30NRD), methyl ammonium bromide (MABr, Greatcell Solar, 99.5%), 2,2',7,7'-tetrakis[*N*,*N*-di(4-methoxyphenyl)amino]-9,9'-spirobifluorene (Spiro-MeOTAD, Ossila Ltd, 99.5%) and formaminidium iodide (FAI, Greatcell solar, 99.5%) were also used as received. Ultrahigh purity (distilled and deionised) water was used in all experiments.

Hydroxyapatite nanoparticle synthesis

The method used to prepare hydroxyapatite (HAP) was a modification of previous methods[1, 2] $Ca(NO_3)_2{\cdot}4H_2O$ (35.42 g, 0.15 mol)) was added to water (200 mL) in a polypropylene (PP) bottle and the pH was adjusted to 7.4 by addition of NaOH (5.0 M) solution. Separately, $(NH_4)_2HPO_4$ (13.206 g, 0.10 mol) was added to water (200 mL) in a different PP bottle and the pH was adjusted to 4.0 by addition of a few drops of HNO_3 (5.0 M) solution. The $Ca(NO_3)_2{\cdot}4H_2O$ solution was then added dropwise at a constant rate over 2 h to the stirred $(NH_4)_2HPO_4$ solution and the pH adjusted to 10.8. The dispersion was allowed to stir for a further 16 h. The HAP nanoparticles (NPs) were collected by vacuum filtration, rinsed extensively with water and dried at 60 ^oC for 16 h in a vacuum oven.

HAP dispersion preparation

HAP dispersion was prepared by mixing HAP NP powder (0.60 g) with ethylcellulose (0.50 wt.%) in ethanol (5.0 mL) followed by stirring for 10 min at room temperature. The dispersion was then ultra-sonicated for 10 min. Meanwhile, ethylcellulose (0.50 g) was added to ethanol (5.0 mL) and stirred for 20 min at 50 ^{o}C. These two solutions were then mixed together and terpineol (3.50 g) added. The HAP dispersion was stirred at 50 ^{o}C and sonicated for 10 min immediately before used. The HAP dispersion concentration was 5.0 wt.%

TiO_2 scaffold preparation

FTO coated glass slides (2.0 cm x 1.5 cm) were cleaned by sonication in an aqueous Hellmanex solution (2%) at 100 ^{o}C for 15 min followed by extensive rinsing with water, acetone, ethanol and IPA. The FTO/glass slides were dried using a nitrogen stream and further treated under UV irradiation and ozone. TiO_2 dispersion (70 µL, 1:5 in ethanol, 5.0 wt%) was spin-coated onto the slides at 5,000 rpm for 30 s to form a mesoporous scaffold (denoted as mp-TiO_2). The mp-TiO_2 film was sequentially annealed at 125 °C (5 min), 325 °C (5 min), 375 °C (5 min) and 450 °C (30 min). The substrate was subsequently left to cool to room temperature.

HAP/TiO_2 mixed scaffold preparation

The two mixed HAP/TiO_2 scaffolds studied contained nominal HAP concentrations of 30 wt.% or 70 wt.%. Accordingly, HAP NP dispersion (5.0 wt.%) (300 mg or 700 mg, respectively, for 30% or 70% HAP scaffold) was mixed with TiO_2 NP dispersion (5.0 wt.%) (700 mg or 300 mg, respectively, for 30% or 70% HAP scaffold) and stirred to obtain the required mixed HAP/TiO_2 dispersion. Sonication was then applied for 15 min. To obtain the mixed scaffold a portion of the mixed dispersion (70 µL) was spin-coated onto the FTO substrate at 5000 rpm for 30 s and sequentially annealed as described above.

Perovskite film preparation

A PbI_2 solution (1.3 M) was prepared in DMF (950 μL)/DMSO (50 μL) co-solvent blend and 75 μL of the solution dropped onto the FTO/bl-TiO_2/scaffold and then spin-coated at 1500 rpm for 30 s. The substrate was placed on a 70 ^oC hot plate and heated for 1 min and cooled to room temperature. A double cation solution was prepared containing FAI (60 mg, 0.349 mM), MABr (6.0 mg, 0.054 mM) and MACl (6.0 mg, 0.089 mM) in 1.0 mL of IPA. This solution was dropped onto the PbI_2 films and then the substrate was spin-coated at 1500 rpm for 30 s. The substrate was then placed on a 150 ^oC hot plate and annealed for 15 min in a nitrogen filled glovebox. The perovskite (PVK) films were stored in a desiccator over P_2O_5 in the dark until investigation.

Device fabrication

Etched FTO-coated glass substrates (TEC15, ~15 Ω/sq, Nippon Glass) were cleaned by following the procedure described above. To deposit a blocking layer of compact TiO_2 (bl-TiO_2) titanium isopropoxide (0.0672 g) was mixed in 2-methoxy ethanol (0.965 g) and ethanolamine (0.082 g) and 95 μL of the solution was spin-coated at 4000 rpm for 30 s on heated substrates (125 °C). The average bl-TiO_2 thickness was 30 nm. The film was sequentially annealed as described above and was treated by UV ozone for 10 mins after cooling. After cooling, scaffolds were deposited by spin-coating 70 μL of the respective dispersion at 5000 rpm for 30s, followed by the same sequential annealing procedure and UV ozone as described above. The PVK film was then deposited as described above. Then, spiro-MeOTAD solution (90 mg/ml in CBZ, 75 μL) added with TBP, Li-TFSI and FK209 was deposited as the hole transport matrix (HTM) and kept in darkness and dry air. A gold layer was deposited on top of the HTM (80 nm) by thermal evaporation.

Physical measurements

The surface and cross-section morphologies were measured using an Ultra 55 Carl Zeiss Sigma FEG-SEM. XRD profiles were obtained using a Bruker D8 Advance diffractometer (Cu-Kα) with a step size of 0.02°. The films were prepared under a nitrogen atmosphere and encapsulated with a thin layer of PMMA for these experiments. UV-visible spectra were recorded using a Perkin Elmer Lambda 25 spectrometer. Photoluminescence (PL) spectra were obtained using an Edinburgh Instruments FLS980 spectrometer. Measurements were conducted from the FTO side of the glass/FTO/HAP-TiO_2/PVK film and the excitation wavelength was 480 nm. The film thicknesses were measured by SEM and / or stylus profilometry (DEKTAK, Bruker GmBH).

Ultraviolet photoemission spectroscopy (UPS) was performed using a HIS 13 high intensity VUV source (200 mA emission, Focus GmbH) within an ESCA2SR spectrometer (Scienta Omicron GmbH) using He I ($h\nu$ = 21.2 eV) photons. The binding energy scale is referenced to the Fermi energy of gold. Space-charge limiting current (SCLC) measurements using electron-only devices were performed using an FTO/bl-TiO_2/meso-TiO_2-HAP/PVK/PCBM/Au architecture. The PCBM concentration in CBZ used for spin-coating was 8.5 mg/mL.

XPS measurements were performed with either a SPECS or a Kratos Ultra Axis XPS spectrometer, equipped with a monochromated Al Kα X-ray source using X-rays with energy of 1486.7 eV. Binding energies (BEs) were calibrated to C 1s from adventitious carbon at 284.8 eV.[3] All XPS spectra were fitted and analysed using a CasaXPS software, where a Shirley background and pseudo-Voigt (GL(30)) function (30% Lorentzian and 70% Gaussian) were applied.[4]

Adsorption experiments

$Pb(NO_3)_2$ powder (1.28 g, 3.9 mmol) was dissolved in water (800 mL) to obtain a stock Pb^{2+} solution with a concentration of 1000 ppm. Then, dilutions using water were used to obtain the required Pb concentrations. HAP powder was added to the Pb solutions and allowed to equilibrate. To determine the Pb concentration samples were analysed using a calibrated using a Pb ion-selective electrode. The equilibrium adsorption capacity (q_e) was calculated using the following equation[5].

$$q_e = \frac{(C_o - C_e)V}{m} \qquad (1)$$

In the above equation C_e, C_o, V and m are the equilibrium Pb^{2+} concentration, initial Pb^{2+} concentration (mg/L), volume of solution and mass of HAP, respectively.

Device measurements

The current density-voltage (J–V) characteristics were measured using a Keithley 2420 Sourcemeter and 100 mW/cm^2 illumination (AM 1.5G) and a calibrated NREL certified Oriel Si-reference cell. An Oriel SOL3A solar simulator was used for these experiments. Forward and reverse direction sweeps were measured with a sweep rate of 0.20 V/s in ~ 40% relative humidity. The device area was 0.080 cm^2. Unless otherwise stated, metrics quoted for the devices are from reverse scans.

Device failure simulation

The HAP-containing devices for failure simulation had an additional HAP encapsulation layer added. Accordingly, HAP dispersion was spin-coated on a cleaned glass slide at 2500 rpm for 60s to obtain a 20 μm HAP encapsulation layer. To prepare a thicker HAP encapsulation layer (40 μm), a slower spin-coating speed was used (1000 rpm, 60s). After that, the HAP-coated glass underwent annealing at 500 ^{o}C for 15 mins. After cooling, the glass/HAP substrate was placed onto devices such that the HAP was in direct contact with the Au layer of the device. An Ossila epoxy was used to seal the device edges.

The completed (encapsulated) PSCs were then damaged to a similar crack degree with a hammer which was used to break the centre of the glass/photoanode substrate. For two-point break the cells were broken on the top surface as well. These damaged PSCs were then placed in separate beakers (100 mL) filled with water (50 mL) and stirred continually. Samples were taken for analysis at specific times and analysed using either a calibrated Pb ion selective electrode or ICP-AES.

HAP characterisation and Pb uptake

TEM of the crystals is shown in Fig. S1. Whilst the crystals aggregated on drying, close examination reveals individual nanorods (see the insets). The X-ray diffraction profile (Fig. S2) reveals that all the peaks match those reported for HAP[6, 7], which supports attainment of high HAP purity. The FTIR spectrum for HAP (Fig. S3) shows the peaks expected. The main peaks at 1025, 600 and 560 cm^{-1} are due to different bending and stretching modes[7, 8] of PO_4^{3-}.

The adsorption capacity (q_{max}, in mg/g) was calculated from adsorption isotherm data (Fig. S4A) plotted according to Equation 2 (Fig. S4B), which is the linearised version of the Langmuir isotherm equation.

$$\frac{C_e}{q_e} = \frac{C_e}{q_{max}} + \frac{1}{q_{max}b} \qquad (2)$$

For the above equation C_e, q_e and b are the equilibrium concentration of Pb(II) (mg/L), adsorption capacity (mg/g) and the Langmuir constant (L/mg), respectively. The line of best fit gave q_{max} and b values of 1350 mg/g and 0.294 g/mg, respectively. The value for q_{max} obtained in this study is much higher than the values reported by other studies, which ranged from 279 to 750 mg/g[9, 10].

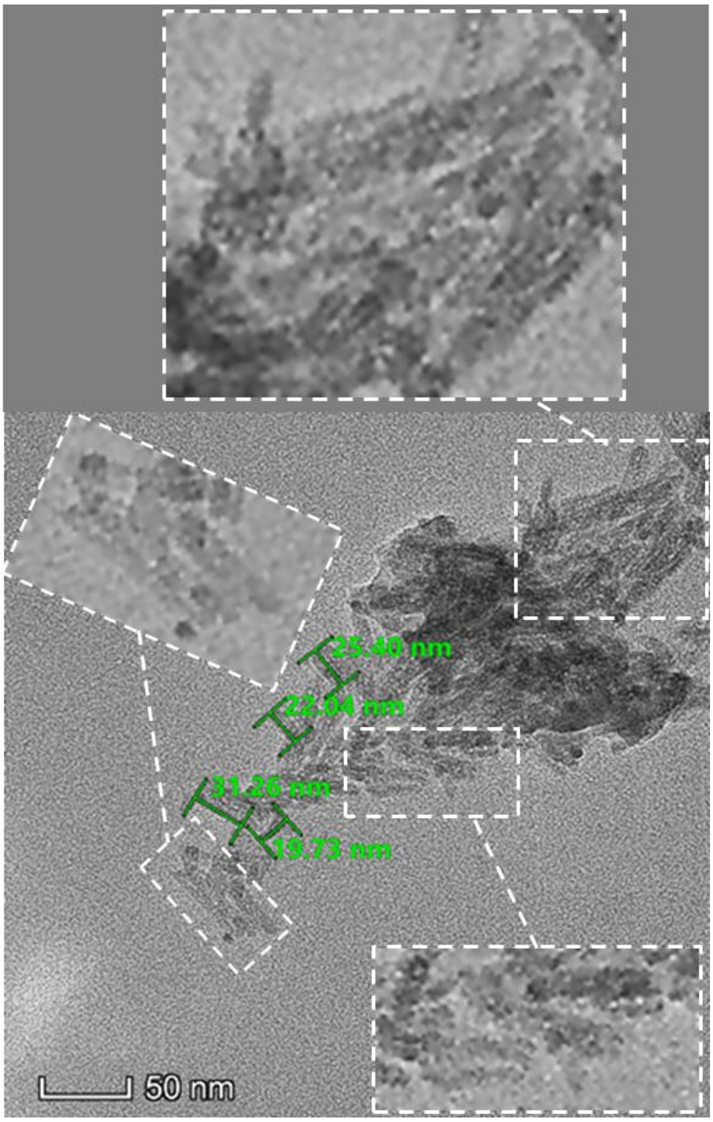

Fig. S1. TEM image of a HAP aggregate of rod-like nanoparticles (NPs). The measurements for several of the nanoparticles are shown. The insets show regions that have been expanded and subjected to despeckle noise reduction (Photoshop) to better show the nanorods.

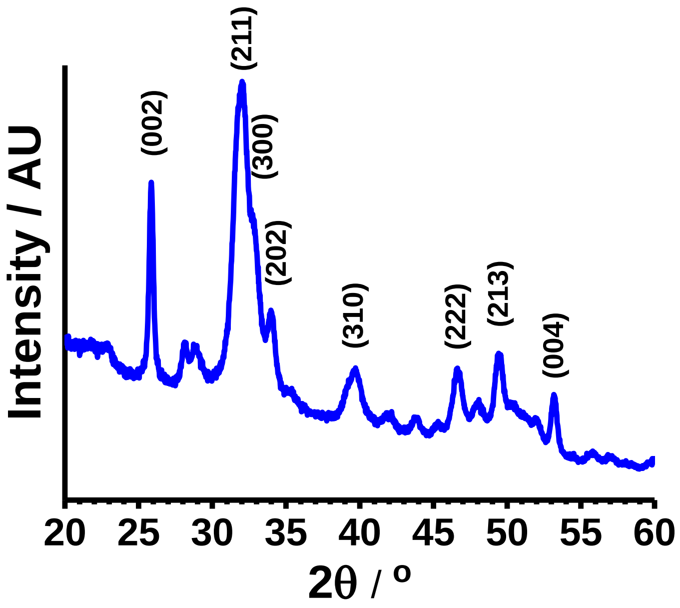

Fig. S2. X-ray diffraction profile for HAP NPs. The assignments are based on those from the literature[11, 12].

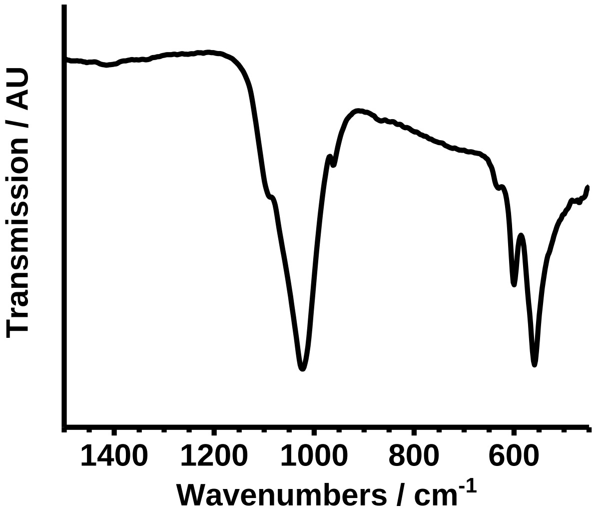

Fig. S3. FTIR spectrum of the HAP NPs. The two main absorption bands are due to PO_4^{3-} (See text).

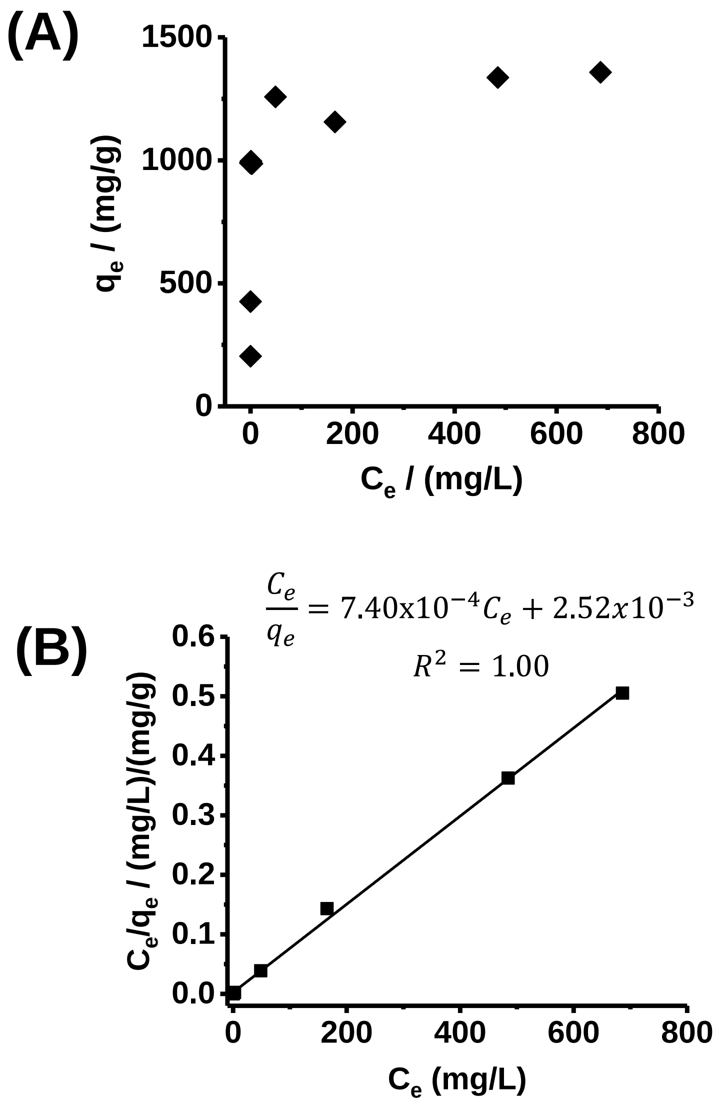

Fig. S4. (A) Adsorption isotherm for Pb with HAP NPs and **(B)** Langmuir fitting for the data from (A). See HAP characterisation and Pb uptake discussion above for more details.

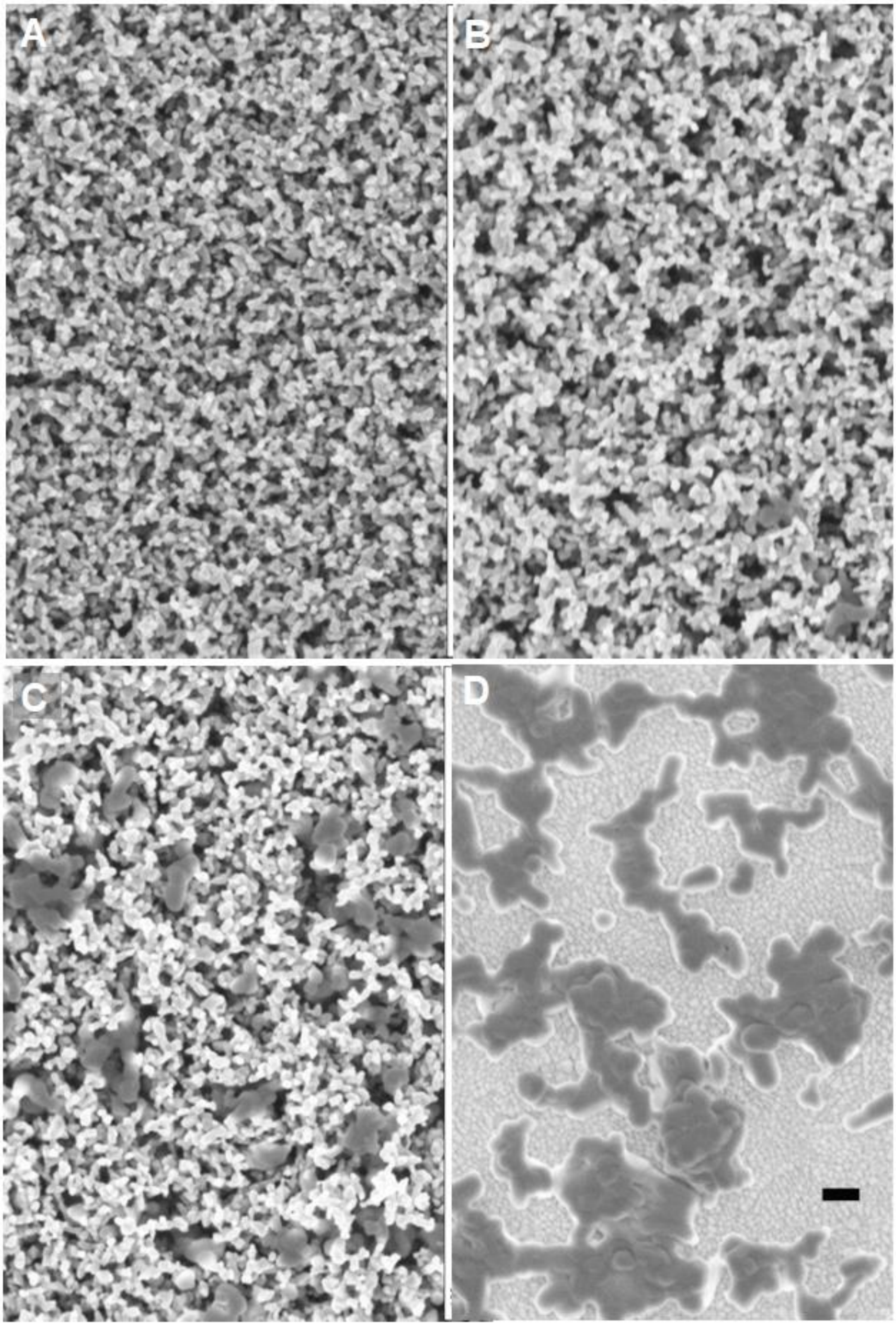

Fig. S5. Large area SEM images for scaffolds containing **(A)** 0%, **(B)** 30%, **(C)** 70% and **(D)** 100% HAP. The TiO_2 and HAP NPs are white dark grey, respectively. The large gaps in (D) are the thin TiO_2 blocking layer on FTO. Scale bar is 100 nm and applies to all images.

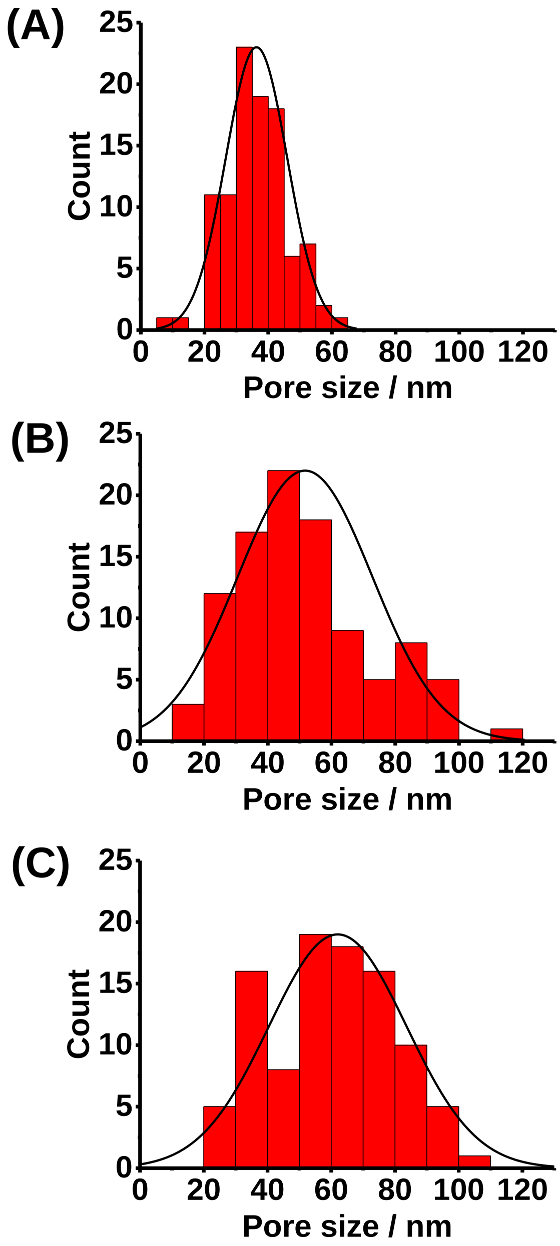

Fig. S6. Pore size distributions for the scaffolds prepared using **(A)** 0%, **(B)** 30% and **(C)** 70% HAP. The pores for the 100% HAP scaffold were very large and interconnected (Fig. S5D) and could not be quantified in a manner that was related to (A) to (C).

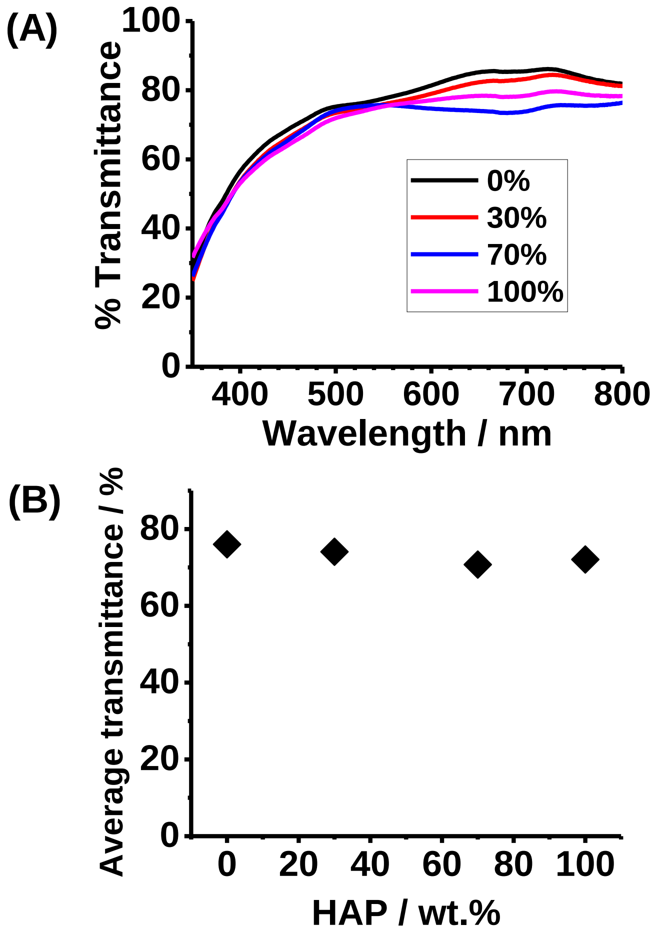

Fig. S7. (A) Transmittance spectra for the various HAP/TiO_2 scaffolds (see legend). **(B)** Average transmittance from the spectra in (A).

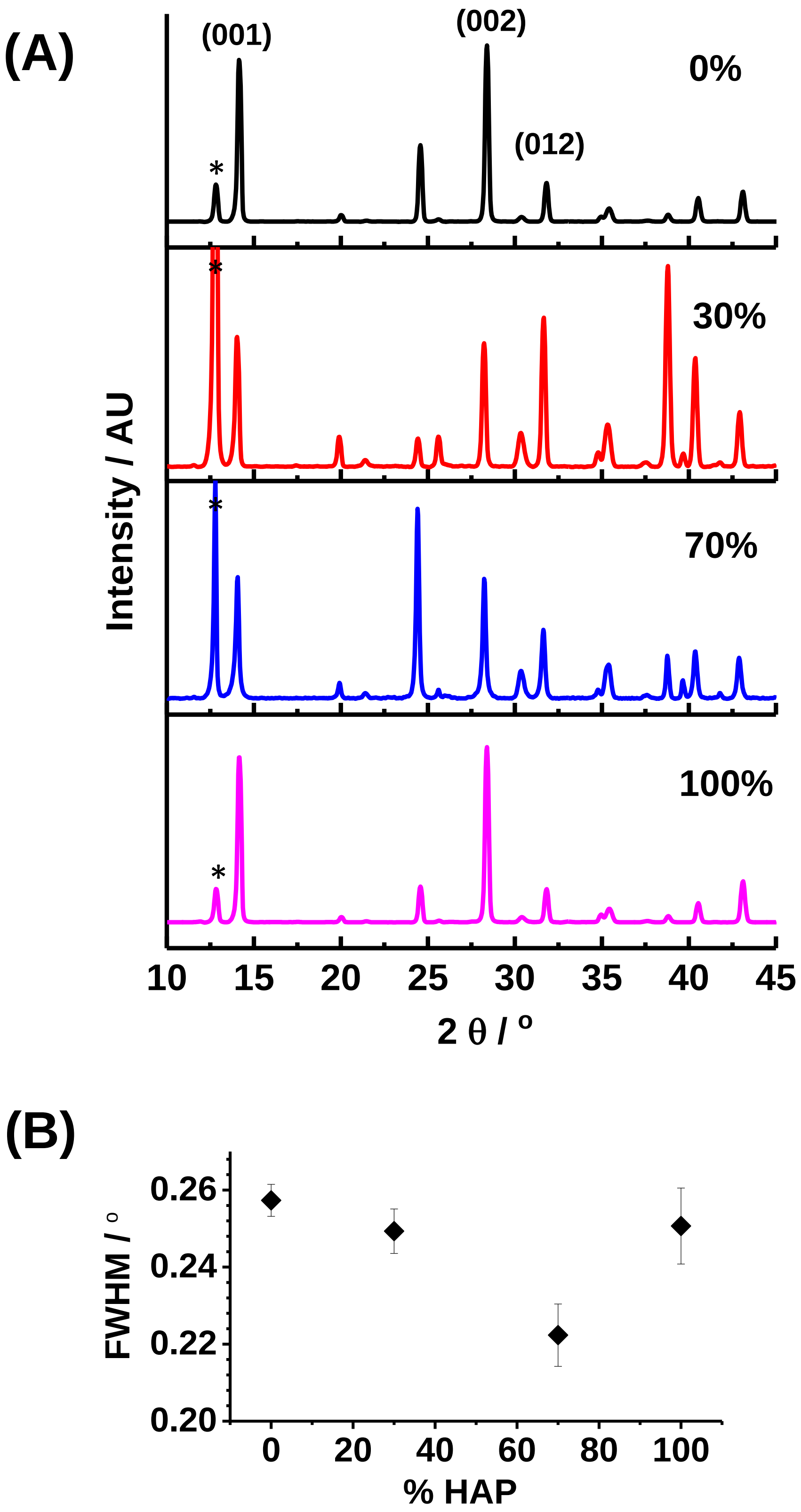

Fig. S8. (A) X-ray diffraction profiles for PVK films prepared using 0% HAP, 30% HAP, 70% HAP and 100 % HAP. The peak labelled with an asterisk is due to PbI_2. The assignments are from Ref. 13 **(B)** Average full-width at half-maximum values from the (001), (002) and (012) peaks in (A).

UPS measurements

UPS measurements were performed for the PVK films prepared using the HAP/TiO_2 scaffolds and the spectra are shown in Fig. S9A and S9B. The energy levels derived from the spectra and the band gap values are show in Fig. S9C. In each case the Fermi level energy (E_F) is closer to the energy of the conduction band minimum (E_{cbm}) than the energy for the valance band maximum (E_{vbm}). Hence, these PVK films are n-doped[14, 15]. This is expected because residual PbI_2 was present as evidenced by the XRD data (Fig. S8A). There is a small downward shift of E_{cbm} and E_{vbm} (by ~ 0.1 – 0.2 eV) as the HAP content increases.

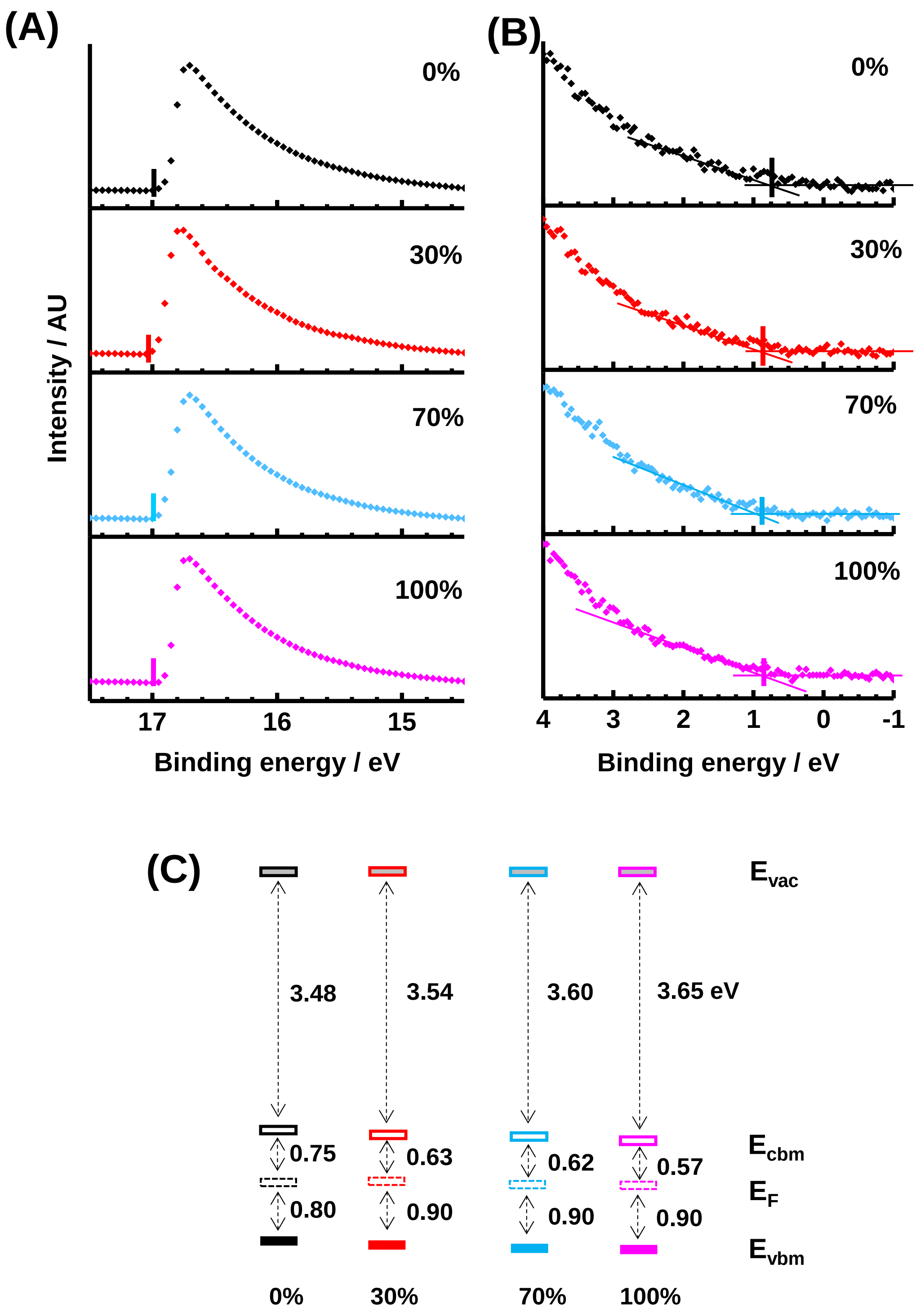

Fig. S9. UPS spectra showing **(A)** the cut-off region ($h\nu$ = 21.22 eV) and **(B)** the valence band edge region for PVK films prepared using 0% HAP, 30% HAP, 70% HAP and 100 % HAP. The work functions were obtained from the difference of $h\nu$ and the cut-off values in (A) and are equal in magnitude to the Fermi energy (E_F). The values for E_{vbm}-E_F were obtained from (B). The conduction band minimum values (E_{Cbm}) were obtained using the sum of E_{vbm} and E_g (from Fig. S13).

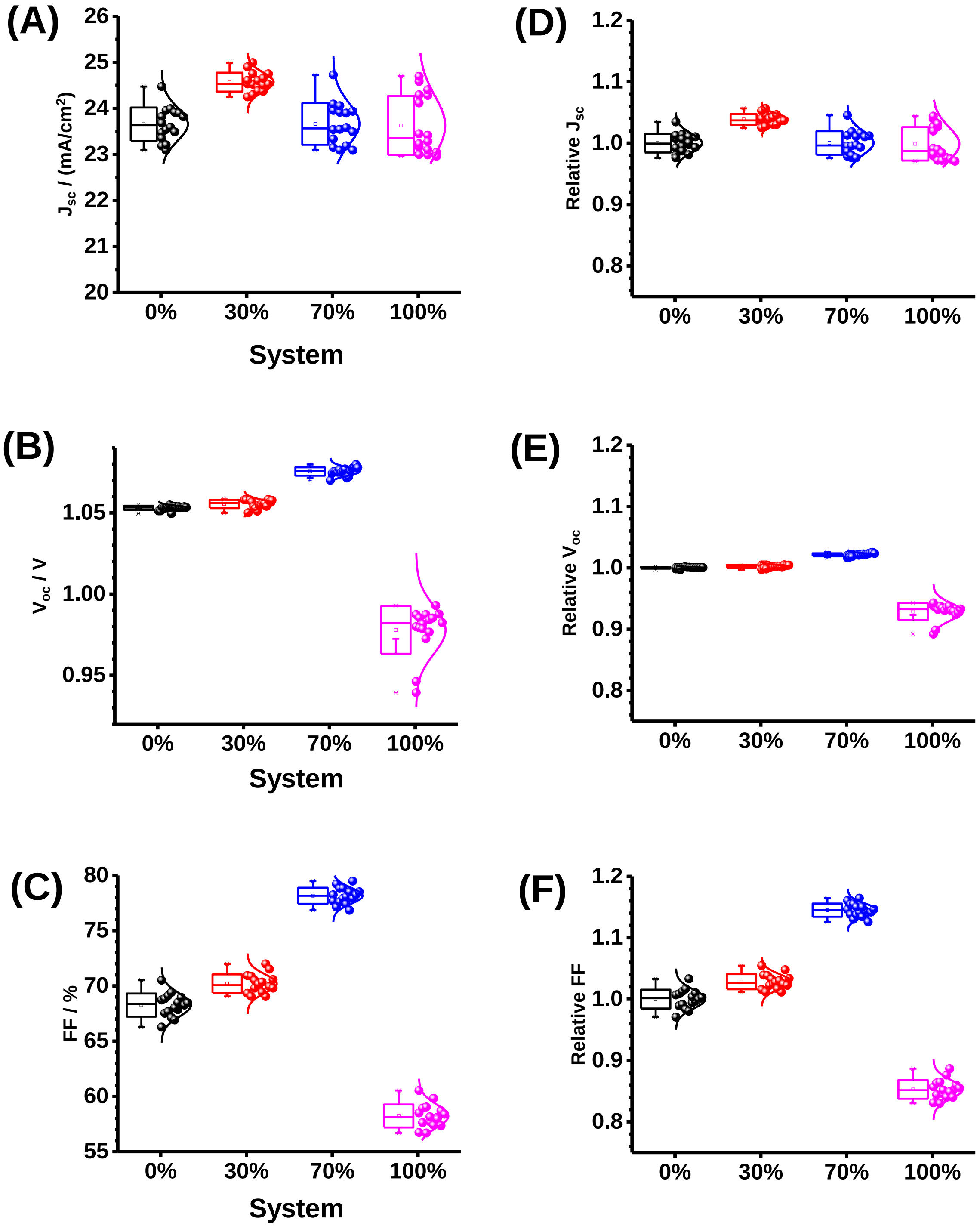

Fig. S10. Measured **(A)** Short circuit current densities, **(B)** open circuit voltages and **(C)** fill factors for the devices prepared using scaffolds containing different HAP concentrations. The relative values of these parameters with respect to the average values for the 0% HAP system are shown in **(D)** – **(F).** These plots reveal the relative importance of each parameter to the PCE data shown in Fig. 3C. It can be seen that the changes in FF and, to a lesser extent V_{oc}, govern the PCE trends of Fig. 3C.

Space-charge limiting current measurements

We fabricated electron-only devices to assess the defect density for the devices using space-charge limiting current measurements (SCLC). The data obtained are shown in Fig. S11A and the device architecture used is depicted in Fig. S11B. There are two regions for these data which are the linear ohmic region and the trap-filled region. The major increase in gradient is due to the traps becoming filled. The number density of defects/traps (N_d) was calculated from the trap-filled voltages (V_{TFL}, see Fig. S11A) and the thicknesses of the photoactive layer (scaffold plus capping layer, L) using the following equation.

$$N_d = \frac{2\varepsilon\varepsilon_o V_{TFL}}{eL^2} \qquad (3)$$

The parameters ε, ε_o and e are the relative dielectric constant of PVK (46.9[16]), dielectric constant of a vacuum and charge of an electron, respectively. The calculated values for N_d are shown in Fig. S11C. These data show that the N_d value is a minimum for the system prepared using 70% HAP.

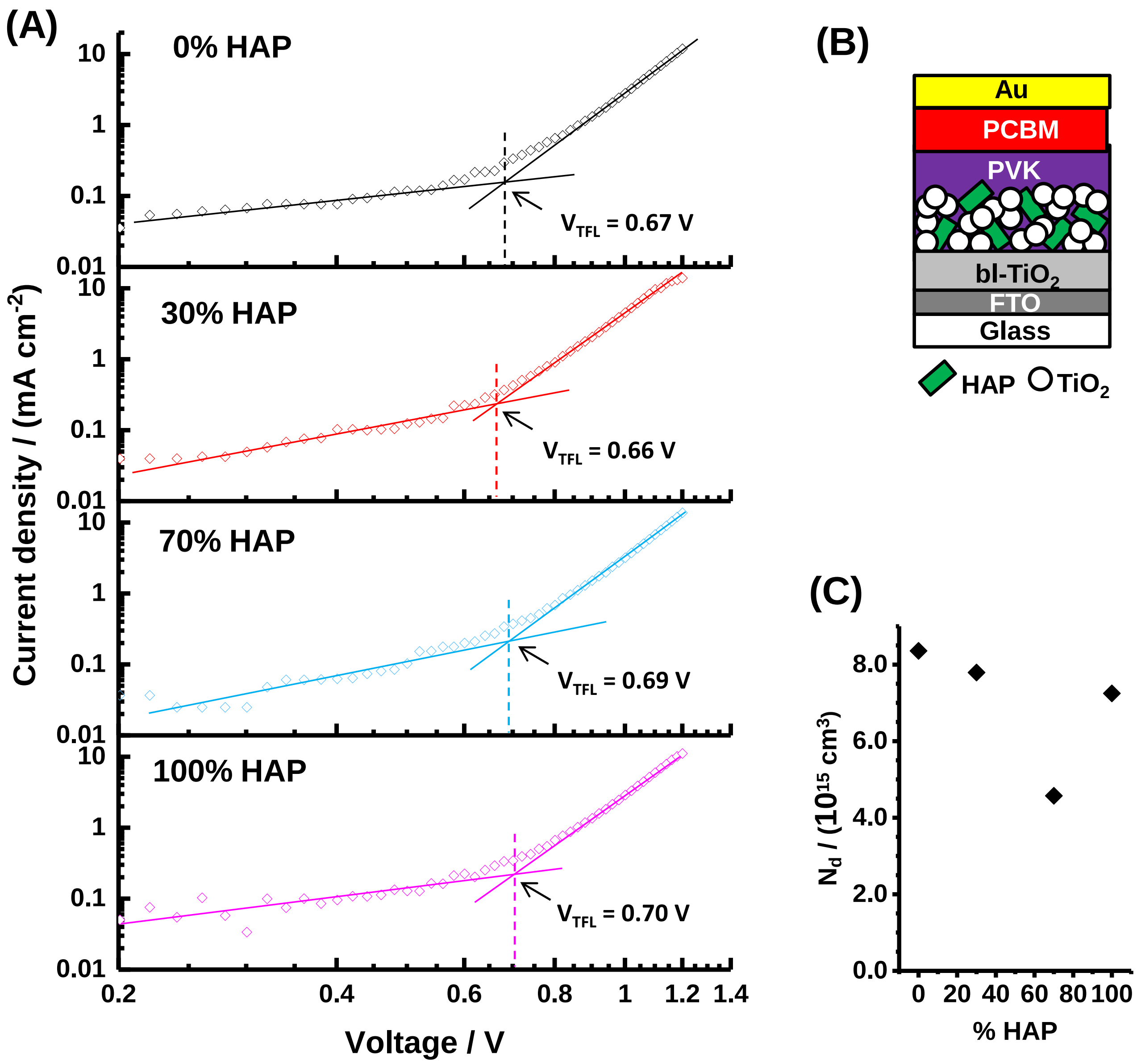

Fig. S11. (A) Space-charge limiting current (SCLC) measurements for electron-only devices using. The trap-filled limit voltages (V_{TFL}) are shown. **(B)** Depiction of the architecture for the electron-only devices. **(C)** Calculated trap density for each of the systems obtained using equation (3).

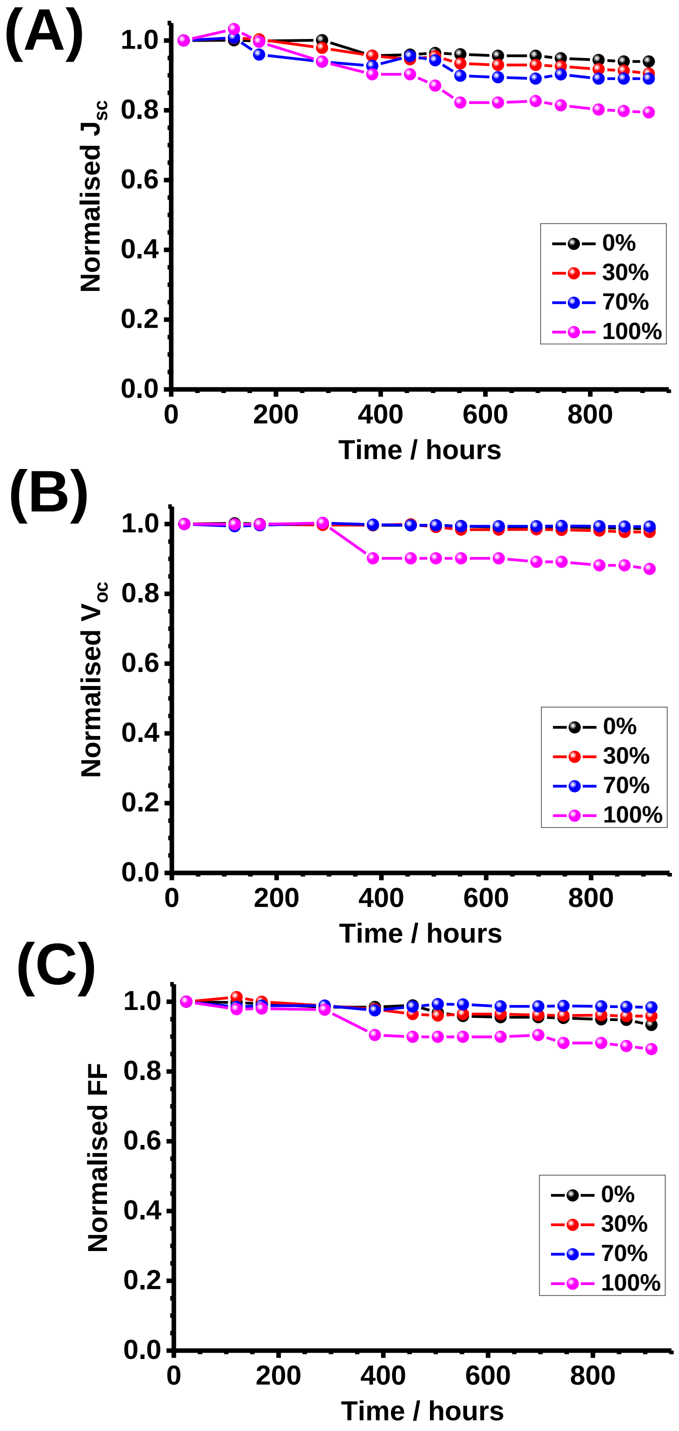

Fig. S12. Evolution of **(A)** short-circuit current densities, **(B)** open circuit voltages and **(C)** fill factors for various systems. The cells were stored under ambient conditions with 40 to 75% RH.

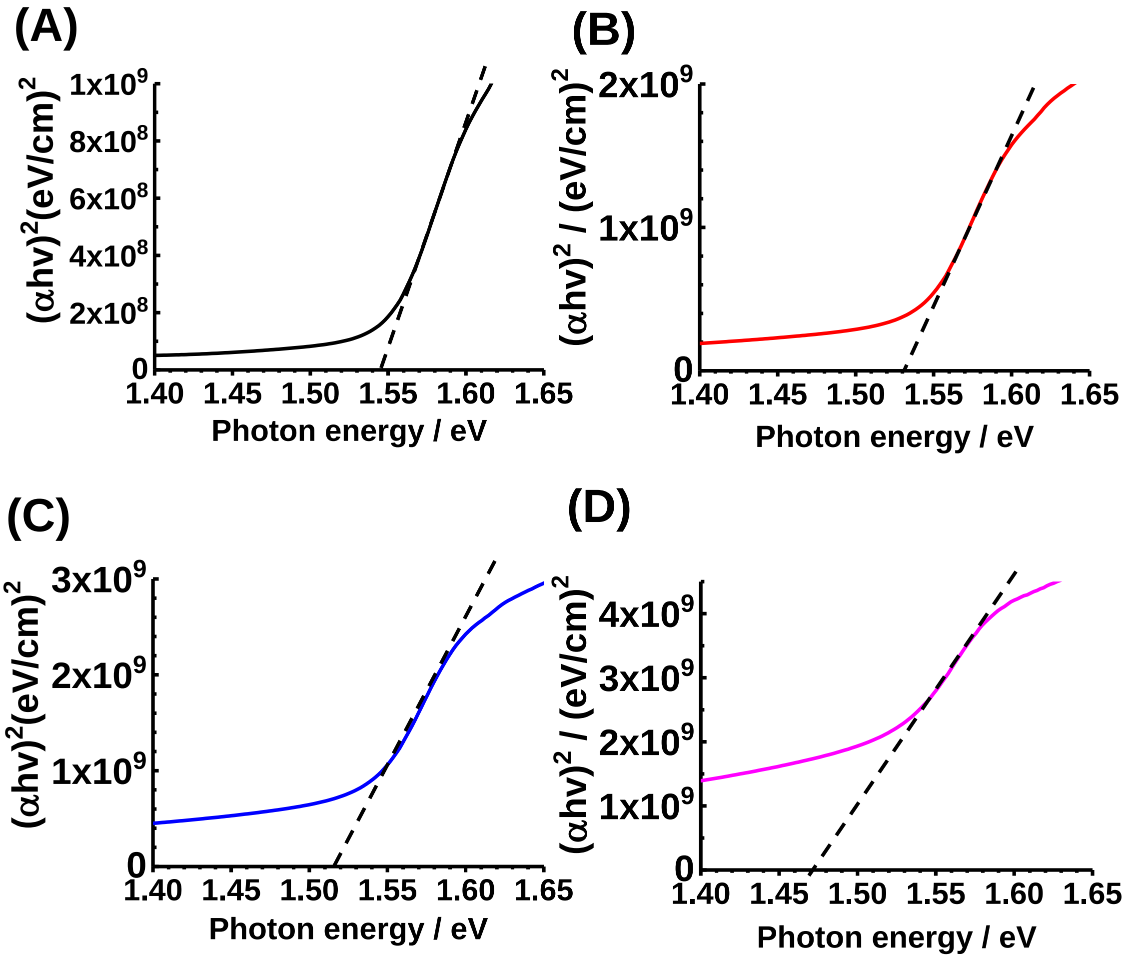

Fig. S13. Tauc plots and estimated optical bandgaps for perovskite films prepared using scaffolds containing **(A)** 0% HAP, **(B)** 30% HAP, **(C)** 70% HAP and **(D)** 100 % HAP. The bandgaps given in the main text.

Probing interactions between HAP and precursors using FTIR spectra of model reactions

In order to test for interactions between HAP and the PVK precursors model experiments were conducted. The reactants in solution were mixed for 2 h at room temperature followed by removal of the solvent in a vacuum oven at 60 °C. The solvents used for (A) and (B) were DMF/DMSO and IPA, respectively. The mass ratios of each species were the same as used for device preparation. The spectrum for HAP + PbI_2 (Fig. S14A) shows that a new peak emerged at 525 cm^{-1}. This is attributed to PO_4^{3-} interacting with Pb^{2+} based on related studies[17, 18]. There is no evidence of an interaction of FAI with HAP from Fig. S14B. It follows that there was an interaction between Pb^{2+} and HAP via the PO_4^{3-} groups. This conclusion is consistent with the XPS data obtained for the broken cell experiments (see Fig. S16).

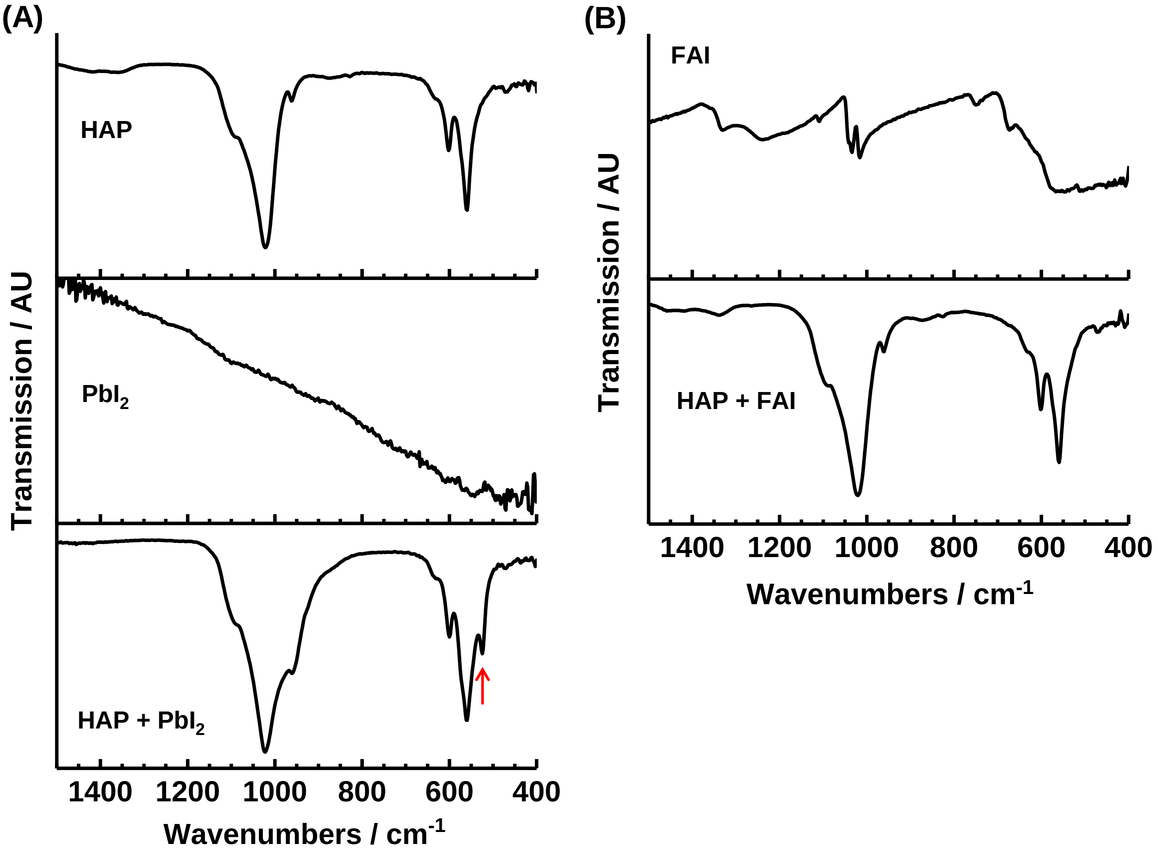

Fig. S14. FTIR spectra obtained from model experiments of **(A)** HAP mixed with PbI_2 and **(B)** HAP mixed with FAI. The spectra for each of the components are also shown. The arrow in the bottom spectrum of (A) is a new peak.

Proposed mechanism for PCE increase for PSCs prepared using HAP/TiO_2 scaffolds

The mechanism by which the PCE reaches a maximum for the 70% system (Fig. 3C) is discussed in the following. The device parameters plotted in Fig. S10D – S10F show that the primary reason for the high PCE is the increase in FF and, to a lesser extent, the V_{oc}. Both of these parameters increase as recombination decreases[19]. The SCLC data (Fig. S11C) show that the 70% HAP device had the lowest trap density (N_d). This low value indicates minimal recombination occurred. This result is attributed to two factors. (1) The 70% system has the largest grain size (754 nm) and hence the lowest proportion of grain boundaries. (2) The 70% system had a near optimum PbI_2/FAPI ratio, and hence residual PbI_2, based on the XRD profile (Fig. S8A) compared to related high-performance PVK films[20]. Residual PbI_2 passivates PVK and reduces recombination[20-22]. The charge extraction for this system remained efficient because the insulating HAP in the mixed scaffold is dispersed vertically within a percolating TiO_2 NP network enabling transport of photo-excited electrons from the PVK to the bl-TiO_2 layer.

In contrast, the 100% HAP has a low PCE primarily due to a low FF and, to a lesser extent, due to a low V_{oc} (see Fig. S10E and S10F) This indicates that recombination was pronounced for this system. It is proposed that recombination is favoured by less efficient charge extraction as a result of the *absence* of the TiO_2 NP scaffold.

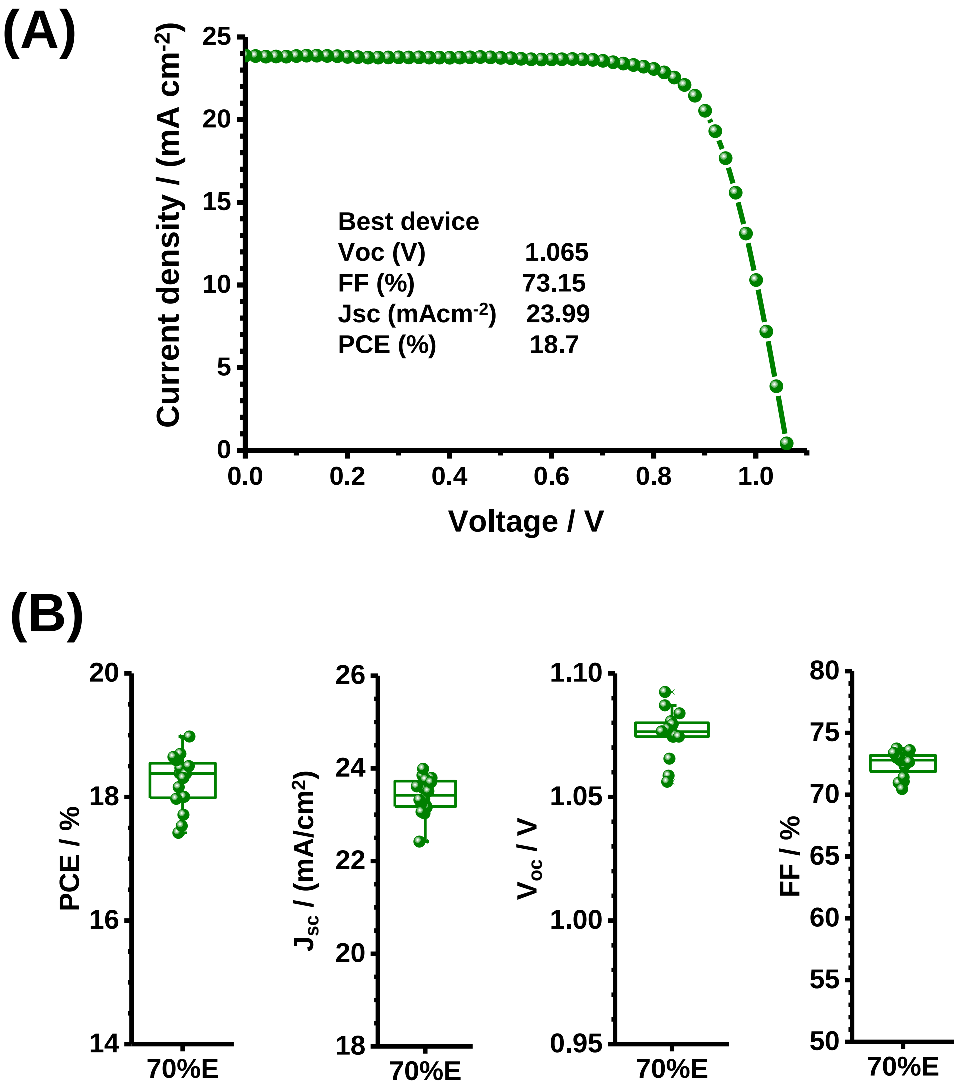

Fig. S15. **(A)** J-V curve for best HAP encapsulated 70% device (termed 70%E_{20} in Fig. 4). **(B)** Box diagrams for the device performance data. The device performance metrics are shown in Table S1.

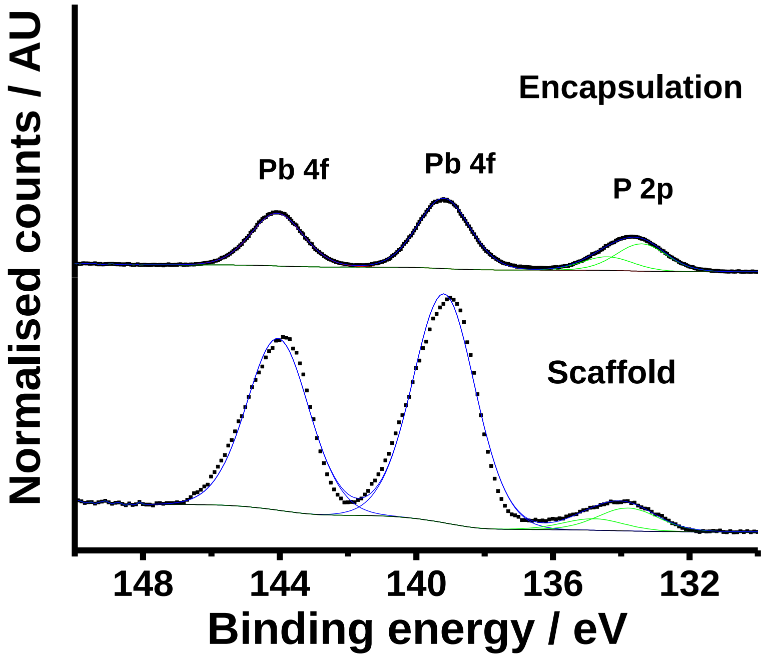

Fig. S16. XPS data for HAP from the encapsulation (top) and scaffold (bottom) layers after immersion of the one-point broken 70%E_{20}-1 cell in water for 24 h (see Fig. 4).

Table S1. Performance data for the perovskite solar cells.

System	Scan direction	V_{oc} [a] / Volts	J_{sc} [b] / (mA cm^{-2})	FF [c] / %	PCE [d] / %	HI [e] / %
0%	Forward	1.053 ± 0.001	23.61 ± 0.34	67.76 ± 0.99	16.85 ± 0.23	1.77
	Reverse	1.053 ± 0.002	23.70 ± 0.40	68.78 ± 0.88	17.16 ± 0.38	
	Average	1.053 ± 0.001	23.66 ± 0.36	68.27 ± 1.05	17.01 ± 0.34	
	Best	1.050	24.48	69.12	**17.76**	
30%	Forward	1.055 ± 0.003	24.60 ± 0.23	69.54 ± 0.38	18.05 ± 0.22	1.74
	Reverse	1.056 ± 0.003	24.54 ± 0.20	70.86 ± 0.62	18.37 ± 0.25	
	Average	1.055 ± 0.003	24.57 ± 0.21	70.20 ± 0.84	18.21 ± 0.28	
	Best	1.058	24.53	71.53	**18.57**	
70%	Forward	1.075 ± 0.003	23.53 ± 0.36	77.75 ± 0.59	19.67 ± 0.39	2.18
	Reverse	1.076 ± 0.002	23.80 ± 0.52	78.57 ± 1.11	20.11 ± 0.42	
	Average	1.075 ± 0.003	23.66 ± 0.45	78.16 ± 0.73	19.89 ± 0.46	
	Best	1.076	24.73	78.85	**20.98**	
100%	Forward	0.974 ± 0.020	23.55 ± 0.65	58.02 ± 1.10	13.30 ± 0.47	2.24
	Reverse	0.982 ± 0.005	23.71 ± 0.67	58.43 ± 1.01	13.60 ± 0.41	
	Average	0.978 ± 0.015	23.63 ± 0.64	58.22 ± 1.04	13.45 ± 0.46	
	Best	0.985	24.70	58.15	**14.15**	
70%E$_{20}$ [f]	Forward	1.076 ± 0.013	23.23 ± 0.45	72.06 ± 1.22	18.01 ± 0.42	2.70
	Reverse	1.075 ± 0.005	23.58 ± 0.26	72.98 ± 0.41	18.51 ± 0.28	
	Average	1.076 ± 0.009	23.41 ± 0.40	72.52 ± 1.00	18.26 ± 0.43	
	Best	1.065	23.99	73.15	**18.70**	

[a] Open circuit voltage. [b] Short-circuit current density. [c] Fill factor. [d] Power conversion efficiency. [e] Hysteresis index = 100 x (PCE_{Rev} – PCE_{Fwd})/PCE_{Rev} , where Rev and Fwd indicate reverse and forward scans, respectively. [f] These devices had the architecture shown in Fig. 4A.

References

1. N. C. C. da Rocha, R. C. de Campos, A. M. Rossi, E. L. Moreira, A. d. F. Barbosa and G. T. Moure, *Environ. Sci. Tech.*, 2002, **36**, 1630-1635.
2. K. Kandori, A. Fujiwara, A. Yasukawa and T. Ishikawa, *Coll. Surf. (A)*, 1999, **150**, 161-170.
3. J. C.-R. Ke, D. J. Lewis, A. S. Walton, B. F. Spencer, P. O'Brien, A. G. Thomas and W. R. Flavell, *J. Mater. Chem. A*, 2018, **6**, 11205-11214.
4. N. Fairley, *CasaXPS manual 2.3. 15*, Acolyte Science, 2009.
5. C. J. Madadrang, H. Y. Kim, G. Gao, N. Wang, J. Zhu, H. Feng, M. Gorring, M. L. Kasner and S. Hou, *ACS Appl. Mater. Interfaces*, 2012, **4**, 1186-1193.
6. S. T. Ramesh, N. Rameshbabu, R. Gandhimathi, P. V. Nidheesh and M. Srikanth Kumar, *Applied Water Science*, 2012, **2**, 187-197.
7. S. Koutsopoulos, *J. Biomed. Mater. Res.*, 2002, **62**, 600-612.
8. B. O. Fowler, *Inorg. Chem.*, 1974, **13**, 194-207.
9. S. H. Jang, Y. G. Jeong, B. G. Min, W. S. Lyoo and S. C. Lee, *J. Hazardous Mater.*, 2008, **159**, 294-299.
10. D. Pham Minh, N. D. Tran, A. Nzihou and P. Sharrock, *Chem. Engineer. J.*, 2013, **232**, 128-138.
11. Y. Han, X. Wang and S. Li, *J. Nanopart. Res.*, 2009, **11**, 1235-1240.
12. S. T. Ramesh, N. Rameshbabu, R. Gandhimathi, P. V. Nidheesh and M. Srikanth Kumar, *Appl. Water Sci.*, 2012, **2**, 187-197.
13. L.-Q. Xie, L. Chen, Z.-A. Nan, H.-X. Lin, T. Wang, D.-P. Zhan, J.-W. Yan, B.-W. Mao and Z.-Q. Tian, *J. Amer. Chem. Soc.*, 2017, **139**, 3320-3323.
14. P. Cui, D. Wei, J. Ji, H. Huang, E. Jia, S. Dou, T. Wang, W. Wang and M. Li, *Nat. Energy*, 2019, **4**, 150-159.
15. H. Xie, X. Liu, L. Lyu, D. Niu, Q. Wang, J. Huang and Y. Gao, *J. Phys. Chem. C.*, 2016, **120**, 215-220.
16. Q. Han, S.-H. Bae, P. Sun, Y.-T. Hsieh, Y. Yang, Y. S. Rim, H. Zhao, Q. Chen, W. Shi, G. Li and Y. Yang, *Adv. Mater.*, 2016, **28**, 2253-2258.
17. M. Kwaśniak-Kominek, J. Matusik, T. Bajda, M. Manecki, J. Rakovan, T. Marchlewski and B. Szala, *Polyhedron*, 2015, **99**, 103-111.
18. V. Laperche and S. J. Traina, *In Adsorption of metals by geomedia: variables, mechanisms and model applications, Academic Press, San Diego*, 1998.
19. M. Stolterfoht, M. Grischek, P. Caprioglio, C. M. Wolff, E. Gutierrez-Partida, F. Peña-Camargo, D. Rothhardt, S. Zhang, M. Raoufi, J. Wolansky, M. Abdi-Jalebi, S. D. Stranks, S. Albrecht, T. Kirchartz and D. Neher, *Adv. Mater.*, 2020, **32**, 2000080.
20. Q. Jiang, Z. Chu, P. Wang, X. Yang, H. Liu, Y. Wang, Z. Yin, J. Wu, X. Zhang and J. You, *Adv. Mater.*, 2017, **29**, 1703852.
21. X.-X. Gao, W. Luo, Y. Zhang, R. Hu, B. Zhang, A. Züttel, Y. Feng and M. K. Nazeeruddin, *Adv. Mater.*, 2020, **32**, 1905502.
22. Q. Chen, H. Zhou, T.-B. Song, S. Luo, Z. Hong, H.-S. Duan, L. Dou, Y. Liu and Y. Yang, *Nano Lett.*, 2014, **14**, 4158-4163.